

Verifying the analogy between transversely coupled spin-1/2 systems and inductively-coupled fluxoniums

Wei-Ju Lin^{1,*}, Hyunheung Cho^{1,*}, Yinqi Chen², Maxim Vavilov², Chen Wang³, and Vladimir Manucharyan^{1,4}

¹*Department of Physics, University of Maryland, College Park, MD, USA*

²*Department of Physics, University of Wisconsin-Madison, Madison, WI, USA*

³*Department of Physics, University of Massachusetts-Amherst, Amherst, MA, USA and*

⁴*Institute of Physics, Ecole Polytechnique Federale de Lausanne, Lausanne, Switzerland*

(Dated: July 23, 2024)

We report a detailed characterization of two inductively coupled superconducting fluxonium qubits for implementing high-fidelity cross-resonance gates. Our circuit stands out because it behaves very closely to the case of two transversely coupled spin-1/2 systems. In particular, the generally unwanted static ZZ -term due to the non-computational transitions is nearly absent despite a strong qubit-qubit hybridization. Spectroscopy of the non-computational transitions reveals a spurious LC -mode arising from the combination of the coupling inductance and the capacitive links between the terminals of the two qubit circuits. Such a mode has a minor effect on our specific device, but it must be carefully considered for optimizing future designs.

I. INTRODUCTION

Engineering on-demand interactions between long-lived quantum bits (qubits) is important for enabling high-fidelity logical gates in future quantum computers. In the case of superconducting qubits [1–3], a common approach is to connect two frequency-detuned qubit circuits via a capacitor and activate the qubit-qubit interaction by microwave drives. A characteristic drawback of such a permanent connection is that it usually leads to a static ZZ -term, which arises from the generally uneven “pressure” on the four computational levels from the higher-energy non-computational levels. This effect can be pronounced not only for weakly-anharmonic transmons [4–9] but also for strongly-anharmonic fluxoniums [10–13]. The magnitude of the static ZZ -term can be suppressed by a variety of tricks, from introducing more complex coupler elements [8, 14–21], including fast-flux-tunable couplers [22], to applying differential AC-stark shifts by off-resonantly driving the non-computational transitions [10]. However, both mitigation strategies increase the complexity of devices and control protocols.

The relatively large ZZ -term in capacitively coupled fluxoniums is related to a general property of transition matrix elements of the charge operator. That is, they are proportional to the transition frequency [23]. Consequently, even if the non-computational states are far detuned from the computational ones, their effect cannot be readily neglected. By contrast, the coupling of fluxoniums via a mutual inductance is governed by the flux operator, and the transition matrix elements do not generally grow with frequency [21, 24]. Combining inductive and capacitive coupling can even lead to completely canceling the static ZZ term [25]. We further explore the inductive coupling of fluxonium qubits for microwave-activated gates.

In this work we describe an inductively-coupled two-fluxonium device. The fluxonium circuits share a common junction, which acts as a linear mutual inductance. The drive is applied via the qubit’s external antenna-like capacitors, which also couple both qubits to a 3D cavity for a joint dispersive readout. The antennas are convenient for creating wireless microwave drives, but they also create capacitive links between circuit terminals, and they need to be taken into account for accurate modeling of the interactions.

Our results can be formulated as follows. A small mutual inductance is indeed sufficient to hybridize qubits with relatively far detuned transitions ($f_{01}^A = 150$ MHz, $f_{01}^B = 230$ MHz) to create an on-demand cross-resonance (CR) interaction (ZX -term) comparable to the Rabi rates of single-qubit gates while the static ZZ -term is suppressed to a few kHz. The capacitance cross-talk does not affect the magnitude of the ZX -term but influences the static ZZ -term. In particular, it creates a previously overlooked LC mode, which, in general, must be taken into account when identifying the spectrum and transition matrix elements of the coupled system. Observation and quantitative modeling of this mode, along with the demonstration of the nearly ideal transversely-coupled spin-1/2 Hamiltonian in the computational subspace, constitute the main focus of the present work.

II. DEVICE AND CIRCUIT MODEL

We start with constructing the full Hamiltonian and demonstrate the analogy between our system and transversely coupled spin-1/2 systems later with the property derived from the device parameters of the Hamiltonian. The Hamiltonian of two inductively and capacitively coupled fluxonium circuits can be written as follows[25].

$$\hat{\mathcal{H}}_{\text{fl}} = \frac{\hat{\mathcal{H}}_A}{h} + \frac{\hat{\mathcal{H}}_B}{h} + J_C \hat{n}_A \hat{n}_B + J_L \hat{\varphi}_A \hat{\varphi}_B. \quad (1)$$

* These authors contributed equally to this work

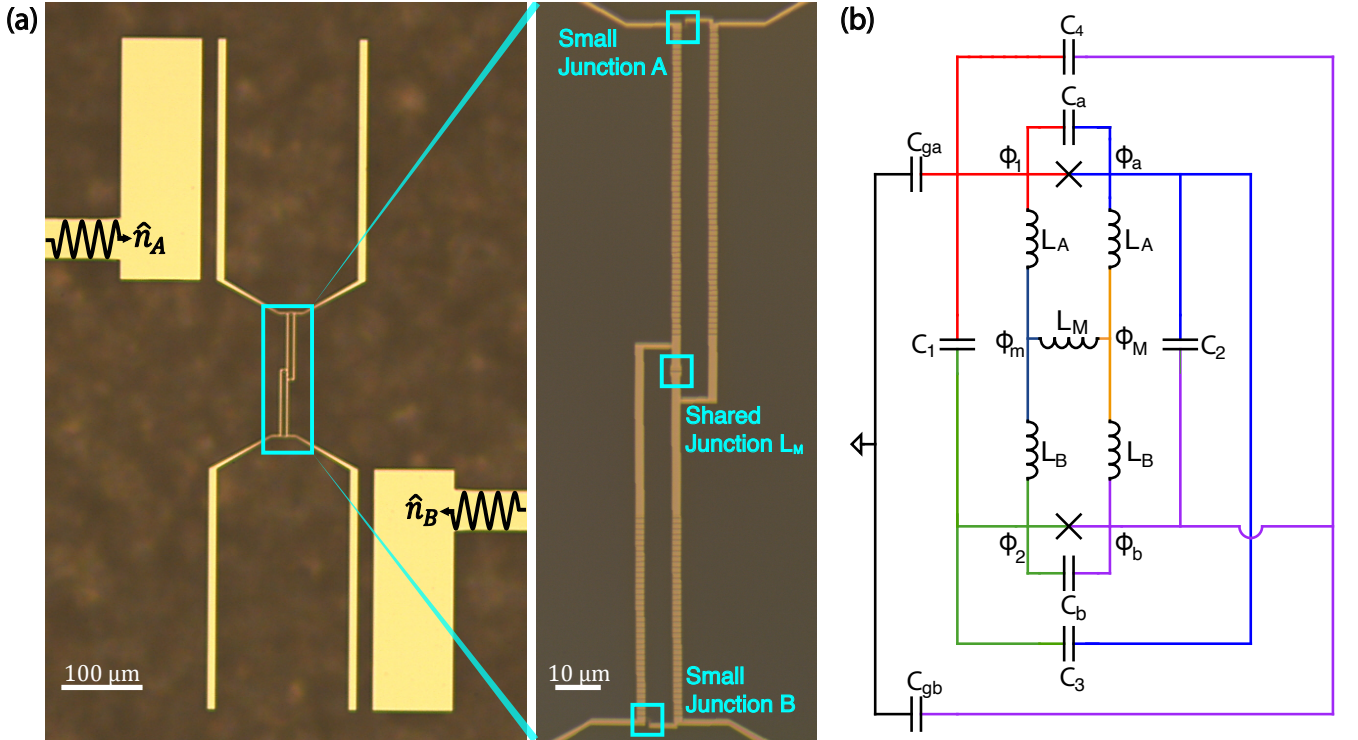


FIG. 1: (a) The optical image of the two-fluxonium inductively coupled device. The joint readout cavity is not shown. The inset shows the mutual inductance L_M and locations of the fluxoniums' small junctions. The left and right lead are designed to drive qubits A and B, respectively, illustrated by the microwave signal symbols with the charge operator $\hat{n}_{A(B)}$. (b) General circuit diagram of the device with false-color representation, taking into account both the inductive coupling and the capacitive cross-talk. Colors correspond to the node flux, ϕ , while L and C denote inductors and capacitors, respectively.

The first two terms describe uncoupled qubits (labeled $\alpha = A, B$),

$$\frac{\hat{H}_\alpha}{\hbar} = 4E_{C,\alpha}\hat{n}_\alpha^2 + \frac{1}{2}E_{L,\alpha}\hat{\varphi}_\alpha^2 - E_{J,\alpha}\cos(\hat{\varphi}_\alpha - \phi_{\text{ext}}), \quad (2)$$

where E_J , E_C , and E_L are the charging, Josephson, and inductive energy, respectively. The capacitive and inductive coupling strengths are J_C and J_L , and the charge operator is $2e\hat{n}$. The flux operator is $(\hbar/2e)\hat{\varphi}$ obey the canonical commutation relation $[\hat{n}, \hat{\varphi}] = i$; a global magnetic field (assuming equal area loops) creates a phase bias ϕ_{ext} . A more thorough circuit analysis for our device shown in Fig. 1(a) reveals the presence of an additional LC -mode as shown in Appendix A based on Fig. 1(b), modifying the system Hamiltonian to

$$\frac{\hat{H}_{\text{full}}}{\hbar} = \frac{\hat{H}_{\text{fl}}}{\hbar} + f_{LC}\hat{a}^\dagger\hat{a} - i \sum_{\alpha=A,B} g_\alpha\hat{n}_\alpha(\hat{a} - \hat{a}^\dagger). \quad (3)$$

\hat{a} , and \hat{a}^\dagger are the creation and annihilation operators of the bosonic mode. The Hamiltonian parameters for the device in question, obtained from the analysis of the measured spectrum, are summarized in Table I. f_{LC} represents the LC -mode frequency. Its coupling strength to

the qubit α is g_α . We also note that the sign of J_L is always positive, while the sign of J_C can either depend on the details of the capacitive cross-talk network. For simplicity of presentation, we are omitting the coupling to the readout mode at about 7.5 GHz, as it has a minor effect on the spectral properties of the two-qubit system.

TABLE I: System parameters of the device

Parameter (GHz)	Qubit A	Qubit B
$E_{J,\alpha}$	5.59	6.27
$E_{L,\alpha}$	0.76	1.16
$E_{C,\alpha}$	0.98	0.99
g_α	0.18	-0.21
f_{LC}		3.22
J_C		-0.038
J_L		0.004

III. SYSTEM CHARACTERIZATION

Fabrication. Our device is fabricated on a 9 mm \times 4 mm, and 430 μm thickness sapphire substrate. The resist is spin-coated onto the diced chip, starting with

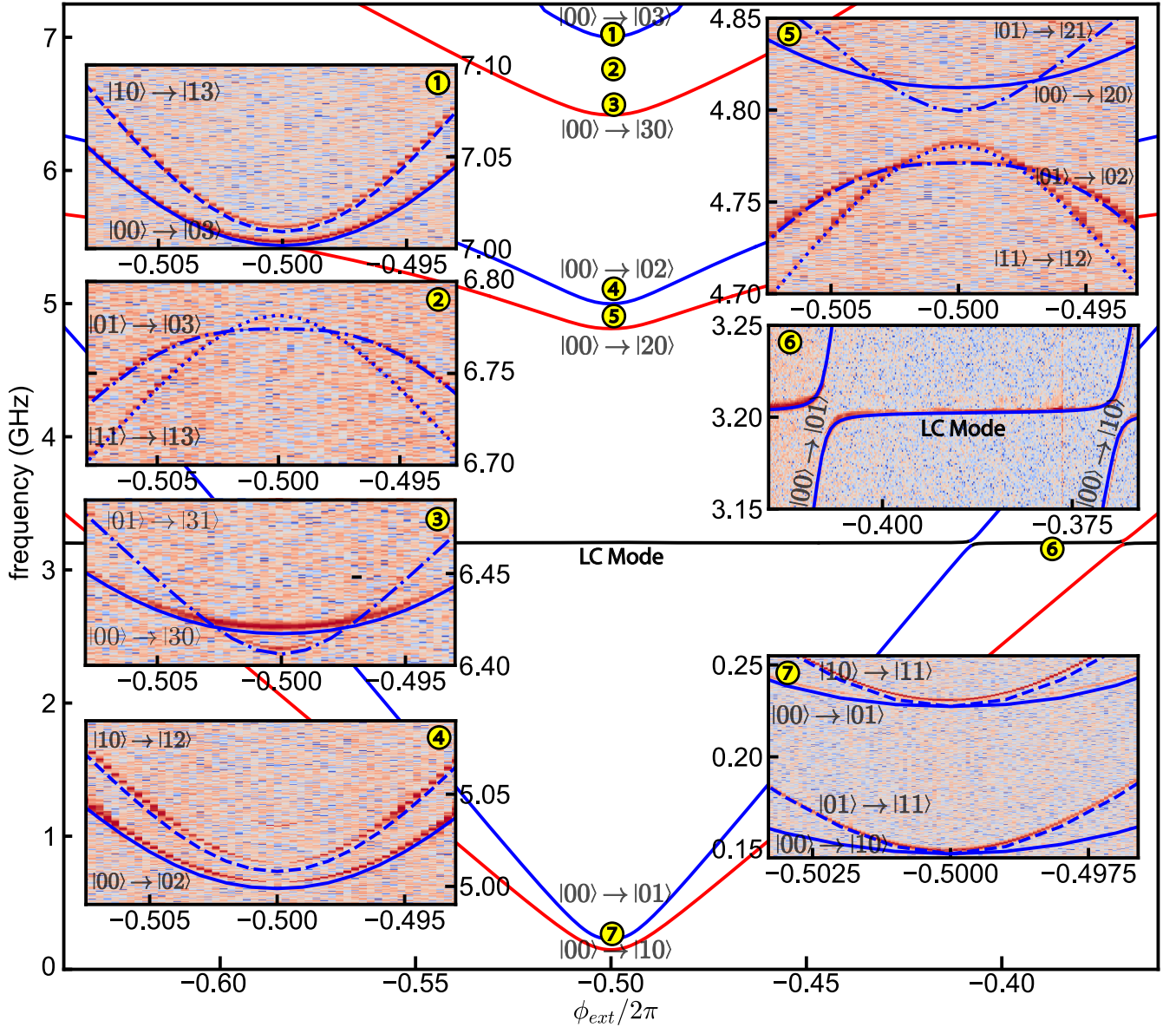


FIG. 2: Fit spectral lines for qubit A (red) and B (blue), assuming adiabatic indexing of the coupled system. The data is shown in insets indexed from ① to ⑦. The computational sub-space is shown in inset ⑦, the stray *LC*-mode and its interaction with the qubits is shown in inset ⑥, and the other insets show various non-computational transitions, all in good agreement with theory.

a layer of MMA resist followed by a layer of PMMA resist. An Elionix system is used for e-beam writing to pattern the design onto the resist-coated chip. After development, a mask is created to outline the qubit structures. The double-angle deposition is carried out using a Plassys deposition system, with aluminum deposited at two angles to form the qubit structures. The process concludes with a lift-off procedure to remove excess material, leaving the patterned qubit devices. More detailed fabrication process is described in [26].

Setup. The measurement setup is comparable to those

detailed in [10], with variations in the room temperature configuration. The chip is placed inside a 3D copper cavity with a resonance frequency of 7.475 GHz, and a linewidth $\kappa/2\pi = 9$ MHz for dispersive joint readout. External driving is introduced into the cavity through two input ports, with the more strongly coupled output port used to measure the transmission signal. The cavity is thermally anchored in the base plate of a dilution refrigerator at a temperature of 14 mK. The device spectrum is measured using a standard two-tone experiment technique, where the cavity readout tone follows the system excitation tone. By fitting the spec-

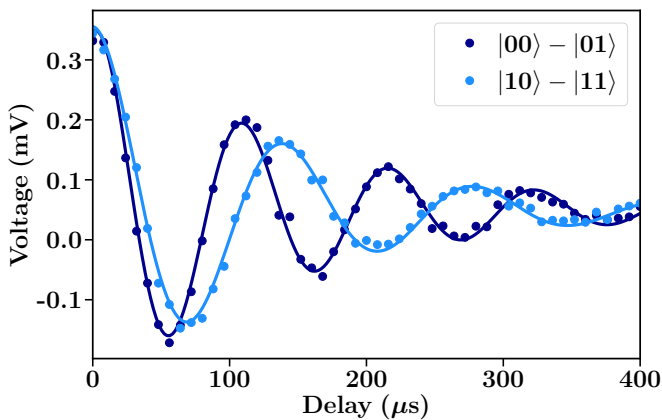


FIG. 3: Ramsey fringe of qubit B conditioned on the state of qubit A. The experiment involves measuring the static ZZ coupling strength with qubit A in the $|0\rangle$ state (dark blue) and in the $|1\rangle$ state (blue). The difference of the two Ramsey frequencies gives the static Z -shift, $\xi_{ZZ}^{\text{static}} = 2$ kHz. The measurement relies on a relatively long decoherence time of the two-qubit system.

trum at various external flux points using the numerical diagonalization of the Hamiltonian presented in Eq. 3, the qubit parameters are extracted, as shown in Table I.

Spectroscopy. Figure 2 shows the device spectrum with theoretical spectrum lines based on qubit parameters in Table I, and the data is shown in the insets from ① to ⑦. Insets ① to ③ show the transitions involving the $|3\rangle$ state, ④ and ⑤ illustrate the transitions involving the $|2\rangle$ state, ⑥ highlights the LC -mode of the system, and inset ⑦ focuses on the transitions involving the $|1\rangle$ state at half flux quantum. The black line in the main figure represents the spurious LC -mode of the system. In the main figure, each index marks the corresponding region for the insets. The two-tone spectroscopy data in Fig. 2 reveals that the $|0\rangle - |1\rangle$ transition frequencies for qubits A and B are 0.15 GHz and 0.23 GHz, respectively. The $|1\rangle - |2\rangle$ transition frequencies are near 4.66 GHz and 4.78 GHz, giving the large anharmonicities of 4.51 GHz for qubit A and 4.54 GHz for qubit B.

Static ZZ -term. Figure 4(a) and (b) present the numerical charge and phase matrix elements, respectively, for the $|0\rangle - |1\rangle$ and $|1\rangle - |2\rangle$ transitions using our bare qubit parameters without any qubit-qubit coupling. We selected the $|1\rangle - |2\rangle$ transition to represent the non-computational space because it exhibits much larger values than other non-computational transitions. Notably, the ratio $|\langle 0|\hat{n}_\alpha|1\rangle/\langle 1|\hat{n}_\alpha|2\rangle| < 1$ implies that achieving strong hybridization of the $|01\rangle$ and $|10\rangle$ states without involving higher energy states is challenging, potentially leading to ZZ interactions if higher energy states are involved. Conversely, the ratio $|\langle 0|\hat{\varphi}_\alpha|1\rangle/\langle 1|\hat{\varphi}_\alpha|2\rangle| > 1$ suggests that the influence of higher energy states is suppressed. This enables strong hybridization between the

$|01\rangle$ and $|10\rangle$ states with negligible ZZ interaction, resembling a pair of transversely coupled spin-1/2.

As a result, our system utilizing direct coupling achieves a low static ZZ value, approximately 2 kHz. To accurately extract this value, we conduct Ramsey experiments on qubit B while setting qubit A to either its ground state or its excited state as shown in Fig. 3. The difference in the frequencies between the two Ramsey fringes is given by ξ_{ZZ}^{static} . We then fit the oscillations to extract the two transition frequencies with a decaying sinusoidal function, and subtract the two frequencies to get the value of ξ_{ZZ}^{static} :

$$\xi_{ZZ}^{\text{static}} = f_{|00\rangle - |01\rangle} - f_{|10\rangle - |11\rangle}. \quad (4)$$

IV. TRUNCATING TO THE 4 COMPUTATIONAL STATES

A. Cross-resonance interaction

Having established the accurate circuit model via spectroscopy, we proceed with truncating the system to its four lowest computational energy states:

$$\hat{\mathcal{H}}_{\text{eff}} = \frac{f_{01}^A}{2} \hat{\sigma}_z^A + \frac{f_{01}^B}{2} \hat{\sigma}_z^B + \frac{\xi_{ZZ}^{\text{static}}}{4} \hat{\sigma}_z^A \hat{\sigma}_z^B + \frac{\hat{\mathcal{H}}_{\text{drive}}}{h}, \quad (5)$$

where h is the Planck constant. $f_{01}^{A,B}$ is the frequency of qubits A and B, and $\hat{\sigma}_z^{A,B}$ are the corresponding Pauli operators. The quantity ξ_{ZZ}^{static} represents the static ZZ interaction rate measured in Fig. 3. The microwave drive Hamiltonian in the computational subspace reduces to

$$\frac{\hat{\mathcal{H}}_{\text{drive}}}{h} = \beta(t) (\xi_A^+ \hat{\sigma}_x^A + \xi_A^- \hat{\sigma}_x^A \hat{\sigma}_z^B + \xi_B^+ \hat{\sigma}_x^B + \xi_B^- \hat{\sigma}_z^A \hat{\sigma}_x^B), \quad (6)$$

where $\beta(t)$ describes the time-dependence of the drive oscillating with frequency f_d equal to one of the qubit frequencies and a smooth amplitude modulation. The real factors ξ_A^+ , ξ_A^- , ξ_B^+ , and ξ_B^- represent effective XI , XZ , IX , and ZX interactions, respectively, which can be written in terms of purely imaginary charge matrix elements as

$$\begin{aligned} i\xi_A^\pm &= \langle 00|\epsilon_A \hat{n}_A + \epsilon_B \hat{n}_B|10\rangle \pm \langle 01|\epsilon_A \hat{n}_A + \epsilon_B \hat{n}_B|11\rangle, \\ i\xi_B^\pm &= \langle 00|\epsilon_A \hat{n}_A + \epsilon_B \hat{n}_B|01\rangle \pm \langle 10|\epsilon_A \hat{n}_A + \epsilon_B \hat{n}_B|11\rangle. \end{aligned} \quad (7)$$

The drive amplitudes ϵ_A and ϵ_B are real and represent two in-phase drives on the two fluxoniums.

B. Two-qubit charge matrix elements

In this section, we describe the charge matrix elements of the transitions within the computational space

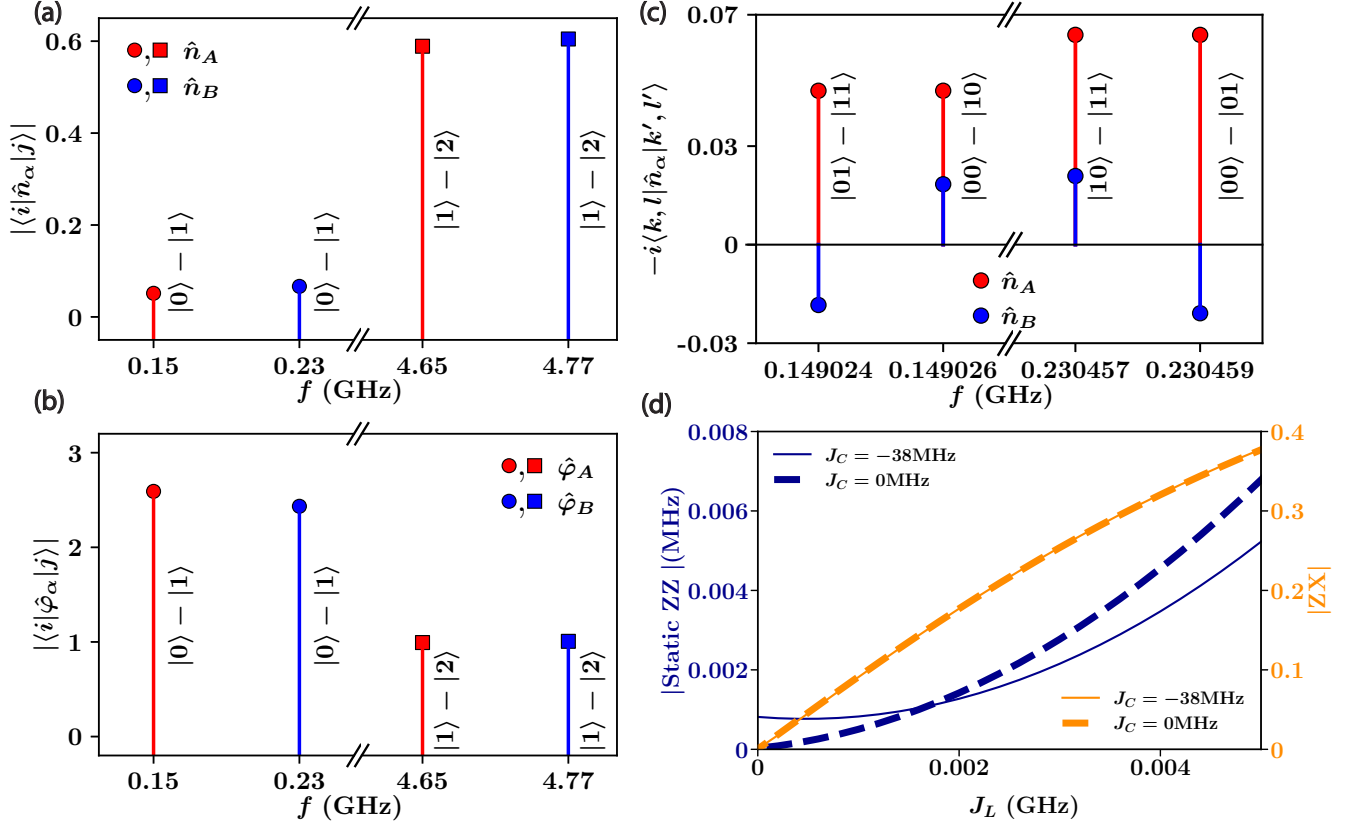


FIG. 4: The charge (a) and phase (b) matrix elements of the two individual qubits without coupling. The qubit parameters are listed in Table I. (c) Two-qubit charge matrix elements for computational transitions. Note, their almost symmetric structure is nearly identical to those of a system of two transversely-coupled spin-half systems. The qubit frequencies are extracted from Ramsey measurements. (d) Numerical values of the static ZZ and the ZX-term. Note the coupling capacitances have no effect on the ZX-term and a minor effect on the ZZ-term.

TABLE II: Charge matrix elements of the transitions inside computational space for charge drives on the two fluxoniums.

$-i\langle kl \hat{n}_j k'l'\rangle$	\hat{n}_A	\hat{n}_B
$ 00\rangle - 10\rangle$	0.046865	-0.018371
$ 01\rangle - 11\rangle$	0.046871	0.018397
$ 00\rangle - 01\rangle$	0.020908	0.063885
$ 10\rangle - 11\rangle$	-0.020883	0.063873

as shown in Fig. 4(c) and Table. II. These matrix elements define the coefficients 7 of the time-dependent Hamiltonian (6). Specifically, we can treat these coefficients as four control knobs: (i) the local drive ϵ_A at the frequency f_{01}^A , (ii) the local drive ϵ_B at the frequency f_{01}^A , (iii) the local drive ϵ_B at the frequency f_{01}^B , and (iv) the local drive ϵ_A at the frequency f_{01}^B . These control knobs provide tuning the XI , XZ , IX , and ZX interaction rates individually, simplifying the operational complexity of CR gates.

A direct drive ϵ_A (ϵ_B) at the frequency f_{01}^A (f_{01}^B) causes the Rabi oscillations in qubit A (B) subspace with

the Rabi frequency determined by the matrix elements $\langle 01|\hat{n}_A|11\rangle$ and $\langle 00|\hat{n}_A|10\rangle$ ($\langle 10|\hat{n}_B|11\rangle$ and $\langle 00|\hat{n}_B|01\rangle$). These pairs of matrix elements have the same magnitude and sign regardless of the state of the other qubit, the condition necessary for single-qubit gates. On the other hand, a cross-resonant drive ϵ_A (ϵ_B) at the frequency f_{01}^B (f_{01}^A) generates rotation of qubit B (A) state with the Rabi frequency proportional to the matrix elements $\langle 10|\hat{n}_A|11\rangle$ and $\langle 00|\hat{n}_A|01\rangle$ ($\langle 01|\hat{n}_B|11\rangle$ and $\langle 00|\hat{n}_B|10\rangle$). Each pair of these matrix elements has the same magnitudes but opposite signs, resulting in state rotations in opposite directions, dependent on the state of qubit A (B). This behavior is suitable for conditional two-qubit gates. The four matrix elements relevant to the cross-resonant drive have magnitudes comparable to those relevant to the direct drive, indicating strong hybridization of computational states. The similarity of matrix elements under strong hybridization indicates the feature of a transversely coupled spin-1/2 system, providing a simple scenario for gate operations with low complexity.

C. Magnitude of the ZX-term

We further investigate the resulting magnitude of the ZX-interaction under the same drive amplitude for single-qubit gates. We evaluate this entangling strength using the following expression:

$$|ZX| = \frac{\left| \xi_B^-(\epsilon_A = \epsilon, \epsilon_B = 0) \right|}{\left| \xi_B^+(\epsilon_A = 0, \epsilon_B = \epsilon) \right|} \quad (8)$$

$$= \frac{\left| \langle 00 | \hat{n}_A | 01 \rangle - \langle 10 | \hat{n}_A | 11 \rangle \right|}{\left| \langle 00 | \hat{n}_B | 01 \rangle + \langle 10 | \hat{n}_B | 11 \rangle \right|},$$

The numerator represents the cross-resonant drive with ϵ_A turned on, and ϵ_B turned off, and the denominator represents the direct drive with ϵ_A turned off, and ϵ_B turned on. Figure 4(d) shows $|ZX|$ as a function of the inductive coupling strength J_L along with the static ZZ phase accumulation rate. We observe that the ZX term grows linearly while the ZZ term grows quadratically in J_L . This facilitates a significant separation of the two frequency scales. For the device in question, a purely inductive coupling of $J_L = 4$ MHz (neglecting the capacitive effects, that is setting $J_C = 0$ and $g_{A(B)} = 0$) results in a relatively small $\xi_{ZZ}^{\text{static}} = 5$ kHz, while the ZX term can readily be close to 0.4. We also observe that the capacitive cross-talk does not affect the ZX-term at all for the device in question and helps suppress the ZZ-term a bit. The measured value of 2 kHz qualitatively agrees with the theoretical prediction.

V. SUMMARY

We have implemented a system of two inductively coupled but capacitively driven fluxonium qubits. The device behaves as a nearly ideal transversely-coupled spin-1/2 system and is thus well suited for all-microwave fixed-frequency cross-resonance two-qubit gates [27, 28]. The CR gate is performed by microwave excitation applied to the control qubit at the frequency of the target qubit and was successfully implemented first in flux qubits [29, 30], and later in transmons [8, 31–35].

It is interesting to note that the values of the qubit frequencies f_{01}^A and f_{01}^B are relatively far from each other than in transmon experiments, which provides more freedom in the choice of circuit parameters. The strength of ZX-interaction is proportional to $J_L/|f_{01}^A - f_{01}^B|$ just like in the case of purely two-level systems. The static ZZ-term is suppressed into the low-kHz range thanks to the combination of a large frequency detuning of the non-computational states and the property of the flux matrix elements in Fig.4(b). Tuning the coupling capacitance can help suppress the ZZ-term to zero, but it also needs to consider the corresponding change of g_A , g_B , and f_{LC} of the stray LC-mode. This case would be a liability in terms of coherent and incoherent errors during gate operations.

ACKNOWLEDGMENTS

This research was supported by the ARO HiPS (contract No. W911-NF18-1-0146) and GASP (contract No. W911-NF23-10093) programs.

Appendix A: Full circuit model analysis

To achieve the Hamiltonian in Eq. 3, we follow the node-flux analysis [36]. We begin by establishing the Lagrangian for the inductive, Josephson junction, and capacitive components. This is followed by applying the Legendre transformation to derive the Hamiltonian.

First, we set up the Lagrangian for the inductance part:

$$\mathcal{L}_{\text{ind}} = - \frac{(\phi_1 - \phi_m)^2 + (\phi_a - \phi_M)^2}{2L_A} - \frac{(\phi_2 - \phi_m)^2 + (\phi_b - \phi_M)^2}{2L_B} - \frac{(\phi_m - \phi_M)^2}{2L_M}, \quad (A1)$$

Each variable $\phi_1, \phi_2, \phi_a, \phi_b, \phi_m$, and ϕ_M corresponds to specific node fluxes in the circuit, as depicted in Fig. 1 (b).

Then, we define the new variables:

$$\phi_A = \phi_a - \phi_1, \quad (A2)$$

$$\phi_B = \phi_2 - \phi_b, \quad (A3)$$

$$\phi_{LC} = \phi_a + \phi_1 - \phi_b - \phi_2, \quad (A4)$$

$$\phi_S = \phi_a + \phi_1 + \phi_b + \phi_2. \quad (A5)$$

Therefore, the new Lagrangian can be written as follows.

$$\mathcal{L}_{\text{ind}} = - \frac{\phi_A^2}{4L_A} - \frac{\phi_B^2}{4L_B} - \frac{\phi_{LC}^2 (L_A + L_B)}{16L_A L_B} + \frac{\phi_A (\phi_M - \phi_m)}{2L_A} + \frac{\phi_B (\phi_m - \phi_M)}{2L_B} - \frac{\phi_{LC} (L_A - L_B) (2\phi_m + 2\phi_M - \phi_S)}{8L_A L_B} + \frac{1}{16} \left(- \frac{8\phi_m^2 - 4\phi_m \phi_S + 8\phi_M^2 - 4\phi_M \phi_S + \phi_S^2}{L_A} \right) - \frac{1}{16} \left(\frac{8\phi_m^2 - 4\phi_m \phi_S + 8\phi_M^2 - 4\phi_M \phi_S + \phi_S^2}{L_B} \right) - \frac{1}{16} \left(\frac{8(\phi_m - \phi_M)^2}{L_M} \right) \quad (A6)$$

We can eliminate ϕ_m and ϕ_M from the equations of motion:

$$\frac{d}{dt} \frac{\partial \mathcal{L}_{\text{ind}}}{\partial \dot{\phi}_k} = \frac{\partial \mathcal{L}_{\text{ind}}}{\partial \phi_k} = 0, \quad (A7)$$

where $k = m$, or M .

Using these relations for ϕ_m and ϕ_M , we can rewrite the Lagrangian as follows:

$$\begin{aligned} \mathcal{L}_{\text{ind}} = & -\frac{(2L_B + L_M)\phi_A^2}{8L_AL_B + 4L_AL_M + 4L_BL_M} \\ & -\frac{L_M\phi_A\phi_B}{4L_AL_B + 2L_AL_M + 2L_BL_M} \\ & -\frac{(2L_A + L_M)\phi_B^2}{8L_AL_B + 4L_AL_M + 4L_BL_M} \\ & -\frac{\phi_{LC}^2}{4(L_A + L_B)}. \end{aligned} \quad (\text{A8})$$

Applying the approximation,

$$L_A, L_B \gg L_M, \quad (\text{A9})$$

we obtain the following Lagrangian for the linear inductance part:

$$\begin{aligned} \mathcal{L}_{\text{ind}} = & -\frac{\phi_A^2}{2(2L_A)} - \frac{\phi_B^2}{2(2L_B)} - \frac{\phi_{LC}^2}{2(2(L_A + L_B))} \\ & -\frac{L_M\phi_A\phi_B}{(2L_A)(2L_B)}. \end{aligned} \quad (\text{A10})$$

Second, we need to set up the Lagrangian for the Josephson junctions, which can be written as:

$$\begin{aligned} \mathcal{L}_{\text{JJ}} = & E_{JA} \cos\left(\frac{2\pi}{\Phi_o}(\phi_A + \Phi_{\text{ext},A})\right) \\ & + E_{JB} \cos\left(\frac{2\pi}{\Phi_o}(\phi_B + \Phi_{\text{ext},B})\right) \end{aligned} \quad (\text{A11})$$

Finally, we set up the Lagrangian for the linear capacitance part:

$$\begin{aligned} \mathcal{L}_{\text{cap}} = & \frac{1}{2} \left[C_a(\dot{\phi}_a - \dot{\phi}_1)^2 + C_b(\dot{\phi}_b - \dot{\phi}_2)^2 \right. \\ & + C_1(\dot{\phi}_1 - \dot{\phi}_2)^2 + C_2(\dot{\phi}_a - \dot{\phi}_b)^2 \\ & + C_3(\dot{\phi}_a - \dot{\phi}_2)^2 + C_4(\dot{\phi}_b - \dot{\phi}_1)^2 \\ & \left. + C_{ga}\dot{\phi}_1^2 + C_{gb}\dot{\phi}_b^2 \right] \end{aligned} \quad (\text{A12})$$

From Eq. A2 to A5, we get the new variables:

$$\dot{\phi}_A = \dot{\phi}_a - \dot{\phi}_1 \quad (\text{A13})$$

$$\dot{\phi}_B = \dot{\phi}_2 - \dot{\phi}_b \quad (\text{A14})$$

$$\dot{\phi}_{LC} = \dot{\phi}_a + \dot{\phi}_1 - \dot{\phi}_2 - \dot{\phi}_b \quad (\text{A15})$$

$$\dot{\phi}_S = \dot{\phi}_a + \dot{\phi}_1 + \dot{\phi}_2 + \dot{\phi}_b \quad (\text{A16})$$

Therefore, the Lagrangian for the linear capacitive part

can be written as follows:

$$\begin{aligned} \mathcal{L}_{\text{cap}} = & \frac{1}{2} \left(C_a\dot{\phi}_A^2 + C_b\dot{\phi}_B^2 \right) \\ & + \frac{1}{8}C_1 \left(\dot{\phi}_A + \dot{\phi}_B - \dot{\phi}_{LC} \right)^2 \\ & + \frac{1}{8}C_2 \left(\dot{\phi}_A + \dot{\phi}_B + \dot{\phi}_{LC} \right)^2 \\ & + \frac{1}{8}C_3 \left(\dot{\phi}_A - \dot{\phi}_B + \dot{\phi}_{LC} \right)^2 \\ & + \frac{1}{8}C_4 \left(-\dot{\phi}_A + \dot{\phi}_B + \dot{\phi}_{LC} \right)^2 \\ & + \frac{1}{32}C_{gb} \left(2\dot{\phi}_B + \dot{\phi}_{LC} - \dot{\phi}_S \right)^2 \\ & + \frac{1}{32}C_{ga} \left(-2\dot{\phi}_A + \dot{\phi}_{LC} + \dot{\phi}_S \right)^2 \end{aligned} \quad (\text{A17})$$

Finally, we define the total Lagrangian to be:

$$\mathcal{L}_{\text{tot}} = \mathcal{L}_{\text{ind}} + \mathcal{L}_{\text{JJ}} + \mathcal{L}_{\text{cap}} \quad (\text{A18})$$

The charge variables can be found following the relation $q_n \equiv \partial\mathcal{L}/\partial\dot{\phi}_n$. The Hamiltonian can be found via the Legendre transformation, giving:

$$\mathcal{H} = \sum_{i=A,B,LC} q_i\dot{\phi}_i - \mathcal{L}_{\text{tot}} \quad (\text{A19})$$

Therefore, we obtain the Hamiltonian:

$$\begin{aligned} \mathcal{H} = & \frac{q_A^2}{2C_A} + \frac{q_B^2}{2C_B} + \frac{q_{LC}^2}{2C_{LC}} + \frac{J_C q_A q_B}{4e^2} \\ & + \frac{\phi_A^2}{2(2L_A)} + \frac{\phi_B^2}{2(2L_B)} + \frac{\phi_{LC}^2}{2(2(L_A + L_B))} + \frac{4e^2 J_L \phi_A \phi_B}{\hbar^2} \\ & + \frac{g_A q_A q_{LC}}{4e^2} + \frac{g_B q_B q_{LC}}{4e^2} \\ & - E_{JA} \cos(\phi_A - \phi_{\text{ext}}) - E_{JB} \cos(\phi_B - \phi_{\text{ext}}). \end{aligned} \quad (\text{A20})$$

There are additional terms of q_S , which is a free variable without ϕ_S . In the final step, the variables are promoted to quantum operators:

$$\begin{aligned} q & \rightarrow \hat{q} = 2e\hat{n} \\ \Phi & \rightarrow \hat{\Phi} = \frac{\hbar}{2e}\hat{\varphi} \end{aligned} \quad (\text{A21})$$

This yields the final Hamiltonian in Eq. 3, agreeing well with the results from scQubits package [37].

Below are the explicit expressions for the coupling or capacitance terms.

The capacitive coupling J_C is as follows:

$$\begin{aligned}
J_C = & ((C_3C_{ga}C_{gb} - (C_{ga} + C_{gb})(C_1C_2 - C_3C_4)) / \\
& ((C_3C_4C_a + C_2C_3(C_4 + C_a) + (C_2 + C_3)C_4C_b \\
& + (C_2 + C_3 + C_4)C_aC_b + C_1(C_3 + C_a)(C_4 + C_b) \\
& + C_1C_2(C_3 + C_4 + C_a + C_b))C_{ga} \\
& + (C_3C_4C_a + C_3C_4C_b + C_3C_aC_b + C_4C_aC_b \\
& + C_3C_aC_{ga} + C_3C_bC_{ga} + C_aC_bC_{ga} \\
& + C_2(C_3 + C_b)(C_4 + C_a + C_{ga}) \\
& + C_1(C_3 + C_a)(C_4 + C_b + C_{ga}) \\
& + C_1C_2(C_3 + C_4 + C_a + C_b + C_{ga}))C_{gb}) \tag{A22}
\end{aligned}$$

The inductive coupling J_L is as follows:

$$J_L = \left(\frac{\hbar}{2e} \right)^2 \frac{L_M}{(2L_A)(2L_B)} \tag{A23}$$

The capacitive coupling g_A is as follows:

$$\begin{aligned}
g_A = & (C_1C_4C_{ga} + (C_1 - C_3 + C_4)C_bC_{ga} \\
& + C_b(-C_3 + C_4 + C_{ga})C_{gb} + C_1(C_4 + C_b + C_{ga})C_{gb} \\
& - C_2(C_3 + C_b)(C_{ga} + C_{gb})) / \\
& ((C_3C_4C_a + C_4C_aC_b + C_3(C_4 + C_a)C_b \\
& + C_2(C_4 + C_a)(C_3 + C_b))C_{ga} \\
& + C_1((C_3 + C_a)(C_4 + C_b) \\
& + C_2(C_3 + C_4 + C_a + C_b))C_{ga} \\
& + C_1((C_3 + C_a)(C_4 + C_b + C_{ga}) \\
& + C_2(C_3 + C_4 + C_a + C_b + C_{ga}))C_{gb} \\
& + (C_aC_b(C_4 + C_{ga}) + C_2(C_3 + C_b)(C_4 + C_a + C_{ga}) \\
& + C_3(C_aC_b + C_4(C_a + C_b) + (C_a + C_b)C_{ga}))C_{gb}) \tag{A24}
\end{aligned}$$

The capacitive coupling g_B is as follows:

$$\begin{aligned}
g_B = & (-((C_2C_4 + (C_2 - C_3 + C_4)C_a)C_{ga} \\
& - (C_a(-C_3 + C_4 + C_{ga}) + C_2(C_4 + C_a + C_{ga}))C_{gb} \\
& + C_1(C_3 + C_a)(C_{ga} + C_{gb})) / \\
& ((C_3C_4C_a + C_2C_3(C_4 + C_a) + (C_2 + C_3)C_4C_b \\
& + (C_2 + C_3 + C_4)C_aC_b + C_1(C_3 + C_a)(C_4 + C_b) \\
& + C_1C_2(C_3 + C_4 + C_a + C_b))C_{ga} \\
& + (C_3C_4C_a + C_3C_4C_b + C_3C_aC_b \\
& + C_4C_aC_b + C_3C_aC_{ga} + C_3C_bC_{ga} + C_aC_bC_{ga} \\
& + C_2(C_3 + C_b)(C_4 + C_a + C_{ga}) \\
& + C_1(C_3 + C_a)(C_4 + C_b + C_{ga}) \\
& + C_1C_2(C_3 + C_4 + C_a + C_b + C_{ga}))C_{gb}) \tag{A25}
\end{aligned}$$

The capacitance for qubit A, C_A , is as follows:

$$\begin{aligned}
C_A = & (2(C_3C_4C_a + C_2C_3(C_4 + C_a) + (C_2 + C_3)C_4C_b \\
& + (C_2 + C_3 + C_4)C_aC_b + C_1(C_3 + C_a)(C_4 + C_b) \\
& + C_1C_2(C_3 + C_4 + C_a + C_b))C_{ga} \\
& + 2(C_3C_4C_a + C_3C_4C_b + C_3C_aC_b + C_4C_aC_b \\
& + C_3C_aC_{ga} + C_3C_bC_{ga} + C_aC_bC_{ga} \\
& + C_2(C_3 + C_b)(C_4 + C_a + C_{ga}) \\
& + C_1(C_3 + C_a)(C_4 + C_b + C_{ga}) \\
& + C_1C_2(C_3 + C_4 + C_a + C_b + C_{ga}))C_{gb}) / \\
& (C_4C_bC_{ga} + C_3(C_4 + C_b)C_{ga} \\
& + C_1(C_2 + C_4 + C_b)C_{ga} + C_b(C_4 + C_{ga})C_{gb} \\
& + C_3(C_4 + C_b + C_{ga})C_{gb} \\
& + C_1(C_2 + C_4 + C_b + C_{ga})C_{gb} \\
& + C_2(C_3 + C_b)(C_{ga} + C_{gb})) \tag{A26}
\end{aligned}$$

The capacitance for qubit B, C_B , is as follows:

$$\begin{aligned}
C_B = & (2(C_3C_4C_a + C_2C_3(C_4 + C_a) + (C_2 + C_3)C_4C_b \\
& + (C_2 + C_3 + C_4)C_aC_b + C_1(C_3 + C_a)(C_4 + C_b) \\
& + C_1C_2(C_3 + C_4 + C_a + C_b))C_{ga} \\
& + 2(C_3C_4C_a + C_3C_4C_b + C_3C_aC_b + C_4C_aC_b \\
& + C_3C_aC_{ga} + C_3C_bC_{ga} + C_aC_bC_{ga} \\
& + C_2(C_3 + C_b)(C_4 + C_a + C_{ga}) \\
& + C_1(C_3 + C_a)(C_4 + C_b + C_{ga}) \\
& + C_1C_2(C_3 + C_4 + C_a + C_b + C_{ga}))C_{gb}) / \\
& ((C_2 + C_3)C_4C_{ga} + (C_2 + C_3 + C_4)C_aC_{ga} \\
& + C_a(C_4 + C_{ga})C_{gb} + C_2(C_4 + C_a + C_{ga})C_{gb} \\
& + C_3(C_4 + C_a + C_{ga})C_{gb} \\
& + C_1(C_2 + C_3 + C_a)(C_{ga} + C_{gb})) \tag{A27}
\end{aligned}$$

The capacitance representing the LC -mode is as follows:

$$\begin{aligned}
C_{LC} = & (2(C_3C_4C_a + C_2C_3(C_4 + C_a) + (C_2 + C_3)C_4C_b \\
& + (C_2 + C_3 + C_4)C_aC_b + C_1(C_3 + C_a)(C_4 + C_b) \\
& + C_1C_2(C_3 + C_4 + C_a + C_b))C_{ga} \\
& + 2(C_3C_4C_a + C_3C_4C_b + C_3C_aC_b + C_4C_aC_b \\
& + C_3C_aC_{ga} + C_3C_bC_{ga} + C_aC_bC_{ga} \\
& + C_2(C_3 + C_b)(C_4 + C_a + C_{ga}) \\
& + C_1(C_3 + C_a)(C_4 + C_b + C_{ga}) \\
& + C_1C_2(C_3 + C_4 + C_a + C_b + C_{ga}))C_{gb}) / \\
& (((C_3 + C_4)C_a + (C_3 + C_4 + 4C_a)C_b \\
& + C_1(C_3 + C_4 + C_a + C_b) \\
& + C_2(C_3 + C_4 + C_a + C_b))C_{ga} \\
& + (C_3C_a + C_4C_a + C_3C_b + C_4C_b + 4C_aC_b \\
& + (C_a + C_b)C_{ga} + C_1(C_3 + C_4 + C_a + C_b + C_{ga}) \\
& + C_2(C_3 + C_4 + C_a + C_b + C_{ga}))C_{gb}) \tag{A28}
\end{aligned}$$

-
- [1] M. H. Devoret and R. J. Schoelkopf, Superconducting Circuits for Quantum Information: An Outlook, *Science* **339**, 1169 (2013).
- [2] G. Wendin, Quantum information processing with superconducting circuits: a review, *Rep. Prog. Phys.* **80**, 106001 (2017).
- [3] M. Kjaergaard, M. E. Schwartz, J. Braumüller, P. Krantz, J. I-J Wang, S. Gustavsson, and W. D. Oliver, Superconducting Qubits: Current State of Play, *Annu. Rev. Condens. Matter Phys.* **11**, 369 (2020).
- [4] K. X. Wei, E. Magesan, I. Lauer, S. Srinivasan, D. F. Bogorin, S. Carnevale, G. A. Keefe, Y. Kim, D. Klaus, W. Landers, N. Sundaresan, C. Wang, E. J. Zhang, M. Steffen, O. E. Dial, D. C. McKay, and A. Kandala, Hamiltonian engineering with multicolor drives for fast entangling gates and quantum crosstalk cancellation, *Phys. Rev. Lett.* **129**, 060501 (2022).
- [5] L. B. Nguyen, Y. Kim, A. Hashim, N. Goss, B. Marinelli, B. Bhandari, D. Das, R. K. Naik, J. M. Kreikebaum, A. N. Jordan, *et al.*, Programmable heisenberg interactions between floquet qubits, *Nature Physics* , 1 (2024).
- [6] B. K. Mitchell, R. K. Naik, A. Morvan, A. Hashim, J. M. Kreikebaum, B. Marinelli, W. Lavrijsen, K. Nowrouzi, D. I. Santiago, and I. Siddiqi, Hardware-efficient microwave-activated tunable coupling between superconducting qubits, *Phys. Rev. Lett.* **127**, 200502 (2021).
- [7] R. Barends, C. M. Quintana, A. G. Petukhov, Y. Chen, D. Kafri, K. Kechedzhi, R. Collins, O. Naaman, S. Boixo, F. Arute, K. Arya, D. Buell, B. Burkett, Z. Chen, B. Chiaro, A. Dunsworth, B. Foxen, A. Fowler, C. Gidney, M. Giustina, R. Graff, T. Huang, E. Jeffrey, J. Kelly, P. V. Klimov, F. Kostritsa, D. Landhuis, E. Lucero, M. McEwen, A. Megrant, X. Mi, J. Mutus, M. Neeley, C. Neill, E. Ostby, P. Roushan, D. Sank, K. J. Satzinger, A. Vainsencher, T. White, J. Yao, P. Yeh, A. Zalcman, H. Neven, V. N. Smelyanskiy, and J. M. Martinis, Diabatic gates for frequency-tunable superconducting qubits, *Phys. Rev. Lett.* **123**, 210501 (2019).
- [8] A. Kandala, K. X. Wei, S. Srinivasan, E. Magesan, S. Carnevale, G. A. Keefe, D. Klaus, O. Dial, and D. C. McKay, Demonstration of a high-fidelity cnot gate for fixed-frequency transmons with engineered zz suppression, *Phys. Rev. Lett.* **127**, 130501 (2021).
- [9] V. Negîrneac, H. Ali, N. Muthusubramanian, F. Battistel, R. Sagastizabal, M. S. Moreira, J. F. Marques, W. J. Vlothuizen, M. Beekman, C. Zachariadis, N. Haider, A. Bruno, and L. DiCarlo, High-fidelity controlled- z gate with maximal intermediate leakage operating at the speed limit in a superconducting quantum processor, *Phys. Rev. Lett.* **126**, 220502 (2021).
- [10] H. Xiong, Q. Ficheux, A. Somoroff, L. B. Nguyen, E. Dogan, D. Rosenstock, C. Wang, K. N. Nesterov, M. G. Vavilov, and V. E. Manucharyan, Arbitrary controlled-phase gate on fluxonium qubits using differential ac stark shifts, *Phys. Rev. Res.* **4**, 023040 (2022).
- [11] Q. Ficheux, L. B. Nguyen, A. Somoroff, H. Xiong, K. N. Nesterov, M. G. Vavilov, and V. E. Manucharyan, Fast logic with slow qubits: Microwave-activated controlled- z gate on low-frequency fluxoniums, *Phys. Rev. X* **11**, 021026 (2021).
- [12] E. Dogan, D. Rosenstock, L. Le Guevel, H. Xiong, R. A. Mencia, A. Somoroff, K. N. Nesterov, M. G. Vavilov, V. E. Manucharyan, and C. Wang, Two-fluxonium cross-resonance gate, *Phys. Rev. Appl.* **20**, 024011 (2023).
- [13] F. Bao, H. Deng, D. Ding, R. Gao, X. Gao, C. Huang, X. Jiang, H.-S. Ku, Z. Li, X. Ma, X. Ni, J. Qin, Z. Song, H. Sun, C. Tang, T. Wang, F. Wu, T. Xia, W. Yu, F. Zhang, G. Zhang, X. Zhang, J. Zhou, X. Zhu, Y. Shi, J. Chen, H.-H. Zhao, and C. Deng, Fluxonium: An alternative qubit platform for high-fidelity operations, *Phys. Rev. Lett.* **129**, 010502 (2022).
- [14] D. C. McKay, S. Filipp, A. Mezzacapo, E. Magesan, J. M. Chow, and J. M. Gambetta, Universal gate for fixed-frequency qubits via a tunable bus, *Phys. Rev. Appl.* **6**, 064007 (2016).
- [15] F. Yan, P. Krantz, Y. Sung, M. Kjaergaard, D. L. Campbell, T. P. Orlando, S. Gustavsson, and W. D. Oliver, Tunable coupling scheme for implementing high-fidelity two-qubit gates, *Phys. Rev. Appl.* **10**, 054062 (2018).
- [16] P. Mundada, G. Zhang, T. Hazard, and A. Houck, Suppression of qubit crosstalk in a tunable coupling superconducting circuit, *Phys. Rev. Appl.* **12**, 054023 (2019).
- [17] Y. Xu, J. Chu, J. Yuan, J. Qiu, Y. Zhou, L. Zhang, X. Tan, Y. Yu, S. Liu, J. Li, F. Yan, and D. Yu, High-fidelity, high-scalability two-qubit gate scheme for superconducting qubits, *Phys. Rev. Lett.* **125**, 240503 (2020).
- [18] M. C. Collodo, J. Herrmann, N. Lacroix, C. K. Andersen, A. Remm, S. Lazar, J.-C. Besse, T. Walter, A. Wallraff, and C. Eichler, Implementation of conditional phase gates based on tunable zz interactions, *Phys. Rev. Lett.* **125**, 240502 (2020).
- [19] Y. Sung, L. Ding, J. Braumüller, A. Vepsäläinen, B. Kannan, M. Kjaergaard, A. Greene, G. O. Samach, C. McNally, D. Kim, A. Melville, B. M. Niedzielski, M. E. Schwartz, J. L. Yoder, T. P. Orlando, S. Gustavsson, and W. D. Oliver, Realization of high-fidelity cz and zz -free iswap gates with a tunable coupler, *Phys. Rev. X* **11**, 021058 (2021).
- [20] L. Ding, M. Hays, Y. Sung, B. Kannan, J. An, A. Di Paolo, A. H. Karamlou, T. M. Hazard, K. Azar, D. K. Kim, B. M. Niedzielski, A. Melville, M. E. Schwartz, J. L. Yoder, T. P. Orlando, S. Gustavsson, J. A. Grover, K. Serniak, and W. D. Oliver, High-fidelity, frequency-flexible two-qubit fluxonium gates with a transmon coupler, *Phys. Rev. X* **13**, 031035 (2023).
- [21] H. Zhang, C. Ding, D. Weiss, Z. Huang, Y. Ma, C. Guinn, S. Sussman, S. P. Chitta, D. Chen, A. A. Houck, J. Koch, and D. I. Schuster, Tunable inductive coupler for high-fidelity gates between fluxonium qubits, *PRX Quantum* **5**, 020326 (2024).
- [22] R. C. Bialczak, M. Ansmann, M. Hofheinz, M. Lenander, E. Lucero, M. Neeley, A. D. O'Connell, D. Sank, H. Wang, M. Weides, J. Wenner, T. Yamamoto, A. N. Cleland, and J. M. Martinis, Fast tunable coupler for superconducting qubits, *Phys. Rev. Lett.* **106**, 060501 (2011).
- [23] K. N. Nesterov, I. V. Pechenezhskiy, C. Wang, V. E. Manucharyan, and M. G. Vavilov, Microwave-activated controlled- z gate for fixed-frequency fluxonium qubits, *Phys. Rev. A* **98**, 030301 (2018).
- [24] X. Ma, G. Zhang, F. Wu, F. Bao, X. Chang, J. Chen,

- H. Deng, R. Gao, X. Gao, L. Hu, H. Ji, H.-S. Ku, K. Lu, L. Ma, L. Mao, Z. Song, H. Sun, C. Tang, F. Wang, H. Wang, T. Wang, T. Xia, M. Ying, H. Zhan, T. Zhou, M. Zhu, Q. Zhu, Y. Shi, H.-H. Zhao, and C. Deng, Native approach to controlled- z gates in inductively coupled fluxonium qubits, *Phys. Rev. Lett.* **132**, 060602 (2024).
- [25] L. B. Nguyen, G. Koolstra, Y. Kim, A. Morvan, T. Chistolini, S. Singh, K. N. Nesterov, C. Jünger, L. Chen, Z. Pedramrazi, B. K. Mitchell, J. M. Kreikebaum, S. Puri, D. I. Santiago, and I. Siddiqi, Blueprint for a high-performance fluxonium quantum processor, *PRX Quantum* **3**, 037001 (2022).
- [26] A. Somoroff, Q. Ficheux, R. A. Mencia, H. Xiong, R. Kuzmin, and V. E. Manucharyan, Millisecond coherence in a superconducting qubit, *Phys. Rev. Lett.* **130**, 267001 (2023).
- [27] G. S. Paraoanu, Microwave-induced coupling of superconducting qubits, *Phys. Rev. B* **74**, 140504 (2006).
- [28] C. Rigetti and M. Devoret, Fully microwave-tunable universal gates in superconducting qubits with linear couplings and fixed transition frequencies, *Phys. Rev. B* **81**, 134507 (2010).
- [29] P. C. de Groot, J. Lisenfeld, R. N. Schouten, S. Ashhab, A. Lupascu, C. J. P. M. Harmans, and J. E. Mooij, Selective darkening of degenerate transitions demonstrated with two superconducting quantum bits, *Nat. Phys.* **6**, 763 (2010).
- [30] J. M. Chow, A. D. Córcoles, J. M. Gambetta, C. Rigetti, B. R. Johnson, J. A. Smolin, J. R. Rozen, G. A. Keefe, M. B. Rothwell, M. B. Ketchen, and M. Steffen, Simple All-Microwave Entangling Gate for Fixed-Frequency Superconducting Qubits, *Phys. Rev. Lett.* **107**, 080502 (2011).
- [31] J. M. Chow, J. M. Gambetta, A. D. Córcoles, S. T. Merkel, J. A. Smolin, C. Rigetti, S. Poletto, G. A. Keefe, M. B. Rothwell, J. R. Rozen, M. B. Ketchen, and M. Steffen, Universal Quantum Gate Set Approaching Fault-Tolerant Thresholds with Superconducting Qubits, *Phys. Rev. Lett.* **109**, 060501 (2012).
- [32] A. D. Córcoles, J. M. Gambetta, J. M. Chow, J. A. Smolin, M. Ware, J. Strand, B. L. T. Plourde, and M. Steffen, Process verification of two-qubit quantum gates by randomized benchmarking, *Phys. Rev. A* **87**, 030301 (2013).
- [33] M. Takita, A. D. Córcoles, E. Magesan, B. Abdo, M. Brink, A. Cross, J. M. Chow, and J. M. Gambetta, Demonstration of Weight-Four Parity Measurements in the Surface Code Architecture, *Phys. Rev. Lett.* **117**, 210505 (2016).
- [34] S. Sheldon, E. Magesan, J. M. Chow, and J. M. Gambetta, Procedure for systematically tuning up cross-talk in the cross-resonance gate, *Phys. Rev. A* **93**, 060302 (2016).
- [35] P. Jurcevic, A. Javadi-Abhari, L. S. Bishop, I. Lauer, D. F. Bogorin, M. Brink, L. Capelluto, O. Günlik, T. Itoko, N. Kanazawa, A. Kandala, G. A. Keefe, K. Kruslich, W. Landers, E. P. Lewandowski, D. T. McClure, G. Nannicini, A. Narasgond, H. M. Nayfeh, E. Pritchett, M. B. Rothwell, S. Srinivasan, N. Sundaresan, C. Wang, K. X. Wei, C. J. Wood, J.-B. Yau, E. J. Zhang, O. E. Dial, J. M. Chow, and J. M. Gambetta, Demonstration of quantum volume 64 on a superconducting quantum computing system, *Quantum Sci. Technol.* **6**, 025020 (2021).
- [36] U. Vool and M. Devoret, Introduction to quantum electromagnetic circuits, *International Journal of Circuit Theory and Applications* **45**, 897 (2017).
- [37] P. Groszkowski and J. Koch, Scqubits: a python package for superconducting qubits, *Quantum* **5**, 583 (2021).